Spin relaxation, Josephson effect, and Yu-Shiba-Rusinov states in superconducting bilayer graphene

Michael Barth and Jacob Fuchs
Institute for Theoretical Physics, University of Regensburg, 93040 Regensburg, Germany

Denis Kochan*
Institute for Theoretical Physics, University of Regensburg, 93040 Regensburg, Germany
and Institute of Physics, Slovak Academy of Sciences, 84511 Bratislava, Slovakia

(Received 3 November 2021; revised 17 February 2022; accepted 19 April 2022; published 5 May 2022)

Bilayer graphene has two nonequivalent sublattices and, therefore, the same adatom impurity can manifest in spectrally distinct ways—sharp versus broad resonances near the charge neutrality—depending on the sublattice it adsorbs at. Employing Green's function analytical methods and the numerical KWANT package, we investigate the spectral and transport interplay between the resonances and superconducting coherence induced in bilayer graphene by proximity to an *s*-wave superconductor. Analyzing doping and temperature dependencies of quasiparticle spin-relaxation rates, energies of Yu-Shiba-Rusinov states, Andreev spectra, and the supercurrent characteristics of Josephson junctions, we find unique superconducting signatures discriminating between resonant and off-resonant regimes. Our findings are in certain aspects going beyond the superconducting bilayer graphene and hold for generic *s*-wave superconductors functionalized by the resonant magnetic impurities.

DOI: 10.1103/PhysRevB.105.205409

I. INTRODUCTION

Microscopic understanding of spin relaxation is a necessary prerequisite for a proper engineering and functionalization of spintronics devices [1]. Promising candidates for such applications are graphene-based systems [2–4] as they offer charge carriers with high mobility, tunable spin-orbit coupling (SOC), and even magnetic-exchange interaction [5]. By graphene-based systems we mean graphene and bilayer graphene (BLG) proximitized by layered van der Waals materials, such as transition metal dichalcogenides (TMDC) [6–10] or magnetic insulators [11–16] that offer new possibilities [17] for exploring (magneto-)transport and (opto-)spintronics phenomena. The new functionality in this regard—triggered by the discovery of the superconductivity in twisted BLG [18,19] and by promising perspectives in superconducting spintronics [20–23]—is the proximity of graphene and BLG with other low-dimensional superconducting materials. Indeed, the proximity-induced superconductivity has been experimentally demonstrated in lateral graphene-based Josephson junctions [24–27], alkaline-intercalated graphite [28–30], and also vertical stacks with the interfacial geometries [31,32].

Here we focus on Bernal stacked BLG in proximity to an *s*-wave superconductor whose quasiparticle spin properties can be altered by impurities depending on the sublattice they hybridize with. Particularly, we look at light adatoms—like hydrogen, fluorine, or copper—and the local magnetic exchange or local SOC interactions that are induced by them. Quite generally [33–35], spin relaxation in the *s*-wave superconductors manifests differently depending on whether the spin-flip scattering is due to SOC (even with regard to time reversal) or magnetic exchange (odd with regard to time reversal). Superconducting coherence enforces composition of the quasiparticle scattering amplitudes in a way that they subtract in the first and sum in the second case what, correspondingly, decreases [36–38] or increases [39,40] superconducting spin relaxation as compared to the normal phase. The enhanced superconducting spin relaxation in the presence of magnetic impurities is known as the Hebel-Slichter-effect [39,41,42], and the temperature dependence of the ratio of the superconducting rate versus its normal-phase counterpart as the Hebel-Slichter peak. The absence of the latter serves' often as a probe of unconventional pairing, however, as scrutinized in Ref. [43], this can be a red herring. Another reason for the breakdown of the Hebel-Slichter effect are resonances caused by a multiple scattering off the underlying Yu-Shiba-Rusinov (YSR) states [44–49]—as was shown in detail for the superconducting single-layer graphene [35]. What happens in BLG and how different sublattice degrees of freedom enter the game is a subject of the present study.

The main goals of our paper are spin, sublattice, and spectral properties of superconducting BLG in the presence of light adatoms that act as magnetic or spin-orbit-coupling resonant scatterers [50–52]. Particularly, (1) we compare temperature and doping dependencies of spin relaxation rates depending on which sublattice an adatom is hybridizing with, (2) analyze the subgap spectral properties in terms of the induced YSR states, and (3) explore critical currents and Andreev bound states (ABS) in the BLG-based superconducting Josephson junctions. Though, some of our findings are general—e.g., the disappearance of the Hebel-Slichter peak when tuning the chemical potential into resonances—and go beyond BLG specifics.

*Corresponding author: denis.kochan@ur.de

The paper is organized as follows; in Sec. II we shortly introduce the model Hamiltonian describing BLG and impurities. The necessary analytical equipment—Green's function, $\mathbb{T}$ matrix, and generalities about the YSR spectra—are presented in Sec. III. Results and other outcomes from the numerical simulations are extensively summarized and qualitatively discussed in Sec. IV. More technical and KWANT implementation aspects are left for the Supplemental Material [53] (see, also, Refs. [35,54–78] therein).

II. MODEL HAMILTONIAN

We consider superconducting Bernal stacked BLG functionalized with light adatoms that hybridize with carbon p_z orbitals in the top layer. Such a system is described by the Hamiltonian

$$H = H_{\mathrm{BLG}} + H_{\mathrm{ada}}, \tag{1}$$

where H_{BLG} describes superconducting BLG host, and the Anderson-type Hamiltonian H_{ada} takes into account local interactions promoted by the adatom. To describe BLG we use the minimal tight-binding Hamiltonian:

$$\begin{aligned} H_{\mathrm{BLG}} = & \sum_{m,n,X,\sigma} (-\gamma_0 \delta_{\langle mn\rangle} - \mu\delta_{mn}) c^{\dagger}_{X,m,\sigma} c_{X,n,\sigma} \\ & + \gamma_1 \sum_{m,\sigma} (c^{\dagger}_{B1,m,\sigma} c_{A2,m,\sigma} + c^{\dagger}_{A2,m,\sigma} c_{B1,m,\sigma}) \\ & + \Delta \sum_{m,X} (c^{\dagger}_{X,m,\uparrow} c^{\dagger}_{X,m,\downarrow} + c_{X,m,\downarrow} c_{X,m,\uparrow}), \end{aligned} \tag{2}$$

where $c_{X,m,\sigma}$ and $c^{\dagger}_{X,m,\sigma}$ are the annihilation and creation operators for an electron with spin σ, located at lattice site m. In order to keep track of the sublattice and layer degrees of freedom, we use along m an additional label $X = \{A1, B1, A2, B2\}$, reserving letter A (B) for the A (B) sublattice and number 1(2) for the bottom (top) layer, respectively; see Fig. 1.

The parameters in Eq. (2) have the standard meaning; $\gamma_0 = 2.6\,\mathrm{eV}$ describes the intralayer nearest neighbor hopping (mimicked by the symbol $\delta_{\langle mn\rangle}$) along the carbon-carbon bond possessing length $a_{cc} = 0.142\,\mathrm{nm}$, $\gamma_1 = 0.34\,\mathrm{eV}$ is an interlayer hopping [75] between the top and bottom carbons separated by a distance $c = 0.335\,\mathrm{nm}$, μ denotes the chemical potential of the system (with zero taken at charge neutrality point of the nonsuperconducting BLG), and, finally, Δ is the global superconducting s-wave pairing induced by a proximity of BLG with a superconductor. In order to capture temperature effects, we assume that Δ follows the conventional BCS dependence well interpolated by the standard formula:

$$\Delta(T) = \Delta_0 \tanh\left[1.74\sqrt{T_c/T - 1}\right]\Theta(T_c - T). \tag{3}$$

For concreteness, we choose $\Delta_0 = 1\,\mathrm{meV}$, giving us the critical temperature $T_c = \Delta_0/(1.76k_{\mathrm{B}}) = 6.953\,\mathrm{K}$ [79]. This slightly elevated value of Δ_0 is a compromise between realistic superconducting proximity in layered carbon systems [80–82] and a numerical capability to handle transport and spectral calculations [83]. The system is illustrated in Fig. 1, along with its normal and superconducting

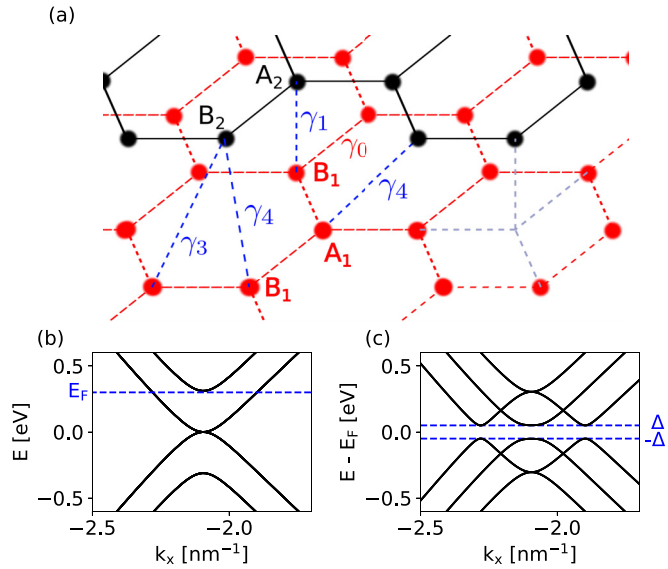

FIG. 1. (a) Schematic illustration of the Bernal-stacked BLG with relevant intra- and interlayer orbital hoppings. Carbons $A1$ and $B2$ which are not coupled via the interlayer coupling γ_1 are conventionally called the low-energy or nondimer sites, and their counterparts $B1$ and $A2$ coupled by γ_1 as the high-energy or dimer sites; we adopt that terminology in what follows. (b) Band structure of BLG around the K point. (c) Quasiparticle band structure of the superconducting BLG at chemical potential E_F shown in panel (b); for visibility we employed an exaggerated value of $\Delta = 50\,\mathrm{meV}$.

quasiparticle band structures. Two remarks are in order: First, the general BLG Hamiltonian in McClure-Slonczewski-Weiss parametrization [73–76] involves also additional interlayer orbital hoppings γ_3 and γ_4; see Fig. 1. We neglect them in what follows, although we checked that they do not bring new qualitative features—for a quantitative comparison of the simple and full models, see the Supplemental Material [53]. Second, intrinsic SOC of BLG [75] is two orders of magnitude smaller than a typical local SOC induced by adatoms (see Refs. [84–87] and the Appendix); therefore we also neglect in H_{BLG} all the intrinsic SOC contributions of the BLG host.

The adatom Hamiltonian H_{ada} comprises orbital and spin interactions [88,89], i.e.,

$$H_{\mathrm{ada}} = V_o + V_s. \tag{4}$$

Assuming the adatom hosts a single electronic orbital governed by the annihilation and creation operators d and $d^{\dagger}$, the Hamiltonian V_o explicitly reads [84–87]

$$\begin{aligned} V_o = & \sum_{\sigma} [(\varepsilon - \mu) d^{\dagger}_{\sigma} d_{\sigma} + \omega (d^{\dagger}_{\sigma} c_{\star\sigma} + c^{\dagger}_{\star\sigma} d_{\sigma})] \\ & + \Delta_d (d^{\dagger}_{\uparrow} d^{\dagger}_{\downarrow} + d_{\downarrow} d_{\uparrow}), \end{aligned} \tag{5}$$

where $c_{\star}$ and $c^{\dagger}_{\star}$ act on the functionalized—dimer or nondimer—carbon site in the top layer. The Anderson-like Hamiltonian V_o is parameterized by the adatom onsite energy ε, the adatom-carbon hybridization ω, and the adatom-located superconducting pairing Δ_d. Its magnitude is not so crucial for the results presented below and therefore, for the sake of

simplicity, we set Δ_d to the corresponding BLG value Δ; see Eq. (3).

For the spin interaction V_s we consider two separate cases: (1) *magnetic exchange* of the adatom d states with a nonitinerant, spin $\frac{1}{2}$, magnetic moment $\mathbf{S}$ that effectively develops on the adatom (through the Hubbard interaction; for details see Ref. [90]) in terms of remaining degrees of freedom dynamically decoupled from d levels, i.e.,

$$V_s^{(1)} = -J\,\mathbf{s}\cdot\mathbf{S}, \tag{6}$$

and (2) *local SOC* Hamiltonian $V_s^{(2)}$, whose explicit but lengthy expression is provided in the Appendix. In the expression for $V_s^{(1)}$, the μth component of the itinerant spin operator $\mathbf{s}$ reads $\mathbf{s}^\mu = d_a^\dagger\,(\boldsymbol{\sigma}^\mu)_{ab}\,d_b$, where $\boldsymbol{\sigma}^\mu$ is μth spin Pauli matrix, and a and b run over $\uparrow$ and $\downarrow$ spin projections of d states. Spin degrees of freedom of the nonitinerant spin, $\Uparrow$ and $\Downarrow$, are introduced such that $\mathbf{S}$ operator is given as a vector of the Pauli matrices acting on these spins. Evaluating the final spin-relaxation rates we trace out $\mathbf{S}$ degrees of freedom; calculation with all details is presented in Ref. [91].

III. GENERAL CONSIDERATIONS: GREEN'S FUNCTIONS AND YSR ENERGIES

A. Green's functions

The starting point for the analytical considerations is the (retarded) Green's resolvent

$$\mathbb{G}(z) = (z - H)^{-1}, \tag{7}$$

where H denotes the full Hamiltonian of the system, e.g., Eq. (1), and $z = E + i\eta$ the complex energy (with a positive infinitesimal imaginary part) measured with respect to the Fermi level μ. In what follows, we show how to obtain superconducting $\mathbb{G}(z)$ in terms of the normal-phase (and hence simpler) Green's function elements and how to calculate the corresponding spin-relaxation rates and YSR spectra. To be concrete, we stick to the case of BLG with adatoms, but the procedure is in fact general, assuming one can split the given Hamiltonian H into an unperturbed part (provisionally called $H_{\rm BLG}$) and a spatially local but not necessarily a pointlike perturbation (in our case $H_{\rm ada}$).

First, defining the Green's resolvent of the unperturbed superconducting system,

$$G(z) = (z - H_{\rm BLG})^{-1}, \tag{8}$$

we can express $\mathbb{G}(z)$ in terms of $G(z)$ by means of the Dyson equation, i.e.,

$$\mathbb{G}(z) = G(z) + G(z)\,H_{\rm ada}\,\mathbb{G}(z) \tag{9}$$

$$= G(z) + G(z)\,\mathbb{T}_{\rm ada}(z)\,G(z) \tag{10}$$

$$= (1 - G(z)\,H_{\rm ada})^{-1}\,G(z). \tag{11}$$

The advantage of the latest expression manifests in the local atomic (tight-binding) basis at which $H_{\rm ada}$ becomes a matrix with few nonzero rows and columns, and hence its inversion is not a tremendous task. In the second equation, Eq. (10), we have defined the $\mathbb{T}$ matrix

$$\mathbb{T}_{\rm ada}(z) = H_{\rm ada}\,(1 - G(z)\,H_{\rm ada})^{-1}. \tag{12}$$

The $\mathbb{T}$ matrix is useful from several points of view. First, inspecting its energy poles within the superconducting gap gives the YSR bound state spectra [92]. Second, knowing the $\mathbb{T}$ matrix one can directly access the spin-relaxation rate $1/\tau_s$ at a given chemical potential μ, temperature T, and the adatom concentration (per number of carbons) $\eta_{\rm ada}$, by evaluating the following expression [34,35]:

$$\frac{1}{\tau_s} = \frac{\iint_{\rm BZ} d\mathbf{k}\,d\mathbf{q}\,|\langle\mathbf{k},\uparrow|\mathbb{T}\,|\mathbf{q},\downarrow\rangle|^2\delta(E_\mathbf{k} - E_\mathbf{q})\big(-\frac{\partial g}{\partial E_\mathbf{k}}\big)}{\frac{\hbar\pi}{A_{\rm uc}\eta_{\rm ada}}\int_{\rm BZ} d\mathbf{k}\big(-\frac{\partial g}{\partial E_\mathbf{k}}\big)}. \tag{13}$$

Therein, the integrations are taken over the first Brillouin zone (BZ) of BLG; $g(E,T) = [e^{E/(k_{\rm B}T)} + 1]^{-1}$ is the Fermi-Dirac distribution whose derivative gives thermal smearing, $A_{\rm uc}$ is the area of the BLG unit cell, and $E_\mathbf{k}$ and $|\mathbf{k},\sigma\rangle$ are, correspondingly, the quasiparticle eigenenergies and eigenstates (normalized to the BLG unit cell) of $H_{\rm BLG}$.

To know the $\mathbb{T}$ matrix, Eq. (12), we need the unperturbed Green's resolvent $G(z)$ of the superconducting host. The next step is the evaluation of $G(z)$ in terms of $g(z)$—the retarded Green's resolvent of BLG in the normal phase. To this end we express $H_{\rm BLG}$, Eq. (2), in the Bogoliubov–de Gennes form (in a basis at which the superconducting pairing becomes a diagonal matrix)

$$H_{\rm BdG} = \begin{pmatrix} h_{\rm BLG} & \Delta \\ \Delta^* & -h_{\rm BLG}^* \end{pmatrix}, \tag{14}$$

where $h_{\rm BLG} = h_{\rm BLG}^* = H_{\rm BLG}(\Delta = 0)$ comprises the nonsuperconducting part of Eq. (2), i.e., an ordinary BLG Hamiltonian held at chemical potential μ. Because of the spatial homogeneity of the s-wave pairing Δ (constant diagonal matrix), the direct inversion of $z - H_{\rm BdG}$ gives

$$G(z) = \begin{pmatrix} g_+(Z) + \frac{z}{Z}g_-(Z) & -\frac{\Delta}{Z}g_-(Z) \\ -\frac{\Delta^*}{Z}g_-(Z) & -g_+(Z) + \frac{z}{Z}g_-(Z) \end{pmatrix}, \tag{15}$$

where

$$Z = \sqrt{z^2 - |\Delta|^2}, \tag{16}$$

$$g_\pm(Z) = \tfrac{1}{2}(Z - h_{\rm BLG})^{-1} \pm \tfrac{1}{2}(-Z - h_{\rm BLG})^{-1}. \tag{17}$$

The proper branch of the complex square root should be chosen in such a way that $\mathrm{Im}\,Z > 0$. So we see that the whole Green's function calculation effectively boils down to an ordinary retarded Green's resolvent of the nonsuperconducting BLG Hamiltonian $h_{\rm BLG}$, i.e., to $g(\pm Z) = (\pm Z - h_{\rm BLG})^{-1}$.

The above equation, Eq. (15), is an operator identity in the Bogoliubov–de Gennes form expressed in a basis in which the pairing component Δ becomes a diagonal matrix. For the later purposes, we would need the matrix elements of $g(z)$ in the local atomic (Wannier) basis, particularly, one matrix element involving the p_z orbital $|\Psi_\star\rangle$ located on carbon site $C_\star$ that hosts the adatom impurity. Such on-site Green's function element—also known as the locator Green's function—reads

$$g_{C_\star}(z) = \langle\Psi_\star|g(z)|\Psi_\star\rangle = \int d\epsilon\,\frac{\varrho_\star(\epsilon+\mu)}{z-\epsilon}, \tag{18}$$

where $\varrho_\star$ is the normal-phase DOS of the unperturbed system projected on the atomic site $C_\star$ and the integration runs

over the corresponding quasiparticle bandwidth. The projected DOS, $\varrho_\star(z) = \sum_{\mathbf{k}} \delta(z - \epsilon_{\mathbf{k}})|\langle\Psi_\star|\mathbf{k}\rangle|^2$, can be routinely computed from the known eigenvalues, $\epsilon_{\mathbf{k}}$, and eigenvectors, $|\mathbf{k}\rangle$, of h_{BLG}.

Up to now the discussion was general without any explicit reference to superconducting or normal-phase BLG Hamiltonians H_{BLG} and $h_{\mathrm{BLG}} = H_{\mathrm{BLG}}(\Delta = 0)$; see Eq. (2). In what follows, we express $g_{C_\star}(z)$ for BLG assuming normal-phase Hamiltonian h_{BLG} with only γ_0 and γ_1 hoppings. In this case, the integral in Eq. (18) can be computed analytically; see Ref. [57]. The resulting $g_{C_\star}(z)$ for the dimer and nondimer $C_\star$ sites are as follows:

$$g^{\mathrm{d}}_{C_\star}(z) = z[F(z^2 + \gamma_1 z) + F(z^2 - \gamma_1 z)], \tag{19}$$

$$g^{\mathrm{nd}}_{C_\star}(z) = g^{\mathrm{d}}_{C_\star}(z) + \gamma_1[F(z^2 + \gamma_1 z) - F(z^2 - \gamma_1 z)], \tag{20}$$

where

$$F(\zeta) = \frac{A_{\mathrm{uc}}}{4\pi v_0^2}\left[I\left(\sqrt{\zeta}/v_0\right) + I\left(-\sqrt{\zeta}/v_0\right)\right], \tag{21}$$

$$I(p) = \frac{1}{2}\ln\left|\frac{\mathrm{Re}^2(p) + \mathrm{Im}^2(p)}{[\Lambda - \mathrm{Re}(p)]^2 + \mathrm{Im}^2(p)}\right| - i\arctan\frac{\mathrm{Re}(p)}{\mathrm{Im}(p)} - i\arctan\frac{\Lambda - \mathrm{Re}(p)}{\mathrm{Im}(p)}. \tag{22}$$

In the above expressions, $A_{\mathrm{uc}} = 3\sqrt{3}\mathrm{a}_{cc}^2/2$ is the area of the BLG unit cell, $v_0 = 3\mathrm{a}_{cc}\gamma_0/2$ and the momentum cutoff $\Lambda = 2\sqrt{\sqrt{3}\pi}/(3\mathrm{a}_{cc})$. Moreover, to keep track on dimensions of different arguments entering functions F and I, we use rather distinct letters, z, ζ, and p, which have, correspondingly, units of energy, energy square, and momentum.

B. Yu-Shiba-Rusinov states and resonances—a toy model and its predictions

In this section, we show under quite general assumptions that resonances caused by magnetic impurities in the nonsuperconducting systems can trigger—after turning into the superconducting phase—a formation of YRS states with energies deep inside the superconducting gap. This phenomenon is quite generic and holds for homogeneous s-wave superconductors with low concentrations of resonant magnetic impurities—assuming the resonance lifetime in the normal phase is larger than the corresponding Larmor precession time, what is the case in single and bilayer graphene.

It is clear from Eqs. (9) and (11) and the definition of the Green's resolvent that the eigenenergies of the full Hamiltonian H can be read off from the singularities of $\mathbb{G}(z) = (z - H)^{-1}$ sending $\eta = \mathrm{Im}\, z$ to zero. We take as a reference some unperturbed superconducting system, e.g., BLG. Let us look at eigenstates of $H = H_{\mathrm{BLG}} + H'_{\mathrm{ada}}$ that can develop inside the superconducting gap of the unperturbed host due to a coupling with a local perturbation centered on a particular atomic site $C_\star$:

$$H'_{\mathrm{ada}} = \sum_\sigma (U + \sigma J) c^\dagger_{\star\sigma} c_{\star\sigma}. \tag{23}$$

The above Hamiltonian represents a perturbation of the Lifshitz-type [93] that is parameterized by the on-site energy U and the magnetic interactions J (the term involving chemical potential μ is in the unperturbed Hamiltonian). This does not cause a fundamental limitation since in certain regimes the Anderson impurity model given by the adatom Hamiltonian

$$H_{\mathrm{ada}} = V_o + V_s^{(1)}, \tag{24}$$

see Eqs. (5) and (6), or even the more general Hubbard impurity model, can be down-folded [90] into the form given by Eq. (23). In what follows, we assume that the orbital energy scale dominates over the magnetic one, i.e., $U^2 \gg J^2$.

It is clear from Eq. (11) that the in-gap states can be extracted from singularities [92] of $(1 - G(z)H'_{\mathrm{ada}})^{-1}$, and therefore one needs to inspect energies $|E| < |\Delta|$ at which the "secular determinant" of the operator $1 - G(z)H'_{\mathrm{ada}}$ turns to zero, i.e.,

$$\det\left[1 - (E - H_{\mathrm{BLG}})^{-1} H'_{\mathrm{ada}}\right] = 0. \tag{25}$$

Since H'_{ada} is located on the atomic site $C_\star$ we just need the corresponding locator of $G(E) = (E - H_{\mathrm{BLG}})^{-1}$, i.e.,

$$G_{C_\star}(E) = \langle\Psi_\star|G(E)|\Psi_\star\rangle. \tag{26}$$

Correspondingly, $\langle\Psi_\star|G(E)|\Psi_\star\rangle$ is a 2×2 matrix in the reduced particle-hole Nambu space [94]. Substituting for $G(E)$ in Eq. (26) the corresponding expression from Eq. (15), we can rewrite $G_{C_\star}(E)$ in terms of the locators of $g_\pm(E)$, see Eq. (17), and even further in terms of the locators of the normal-phase resolvents $(\pm Z(E) - h_{\mathrm{BLG}})^{-1}$, where for the in-gap states $\pm Z(E) = \pm i\sqrt{|\Delta|^2 - E^2}$. The locator that is finally needed to be calculated turns to be the following integral,

$$g_{C_\star}(\pm Z(E)) = \int dx\, \frac{\varrho_\star(x)}{\mu \pm i\sqrt{|\Delta|^2 - E^2} - x} \equiv \gamma(\pm E); \tag{27}$$

see also Eq. (18).

Similarly, the perturbation H'_{ada} turns to be a 2×2 matrix in the particle-hole space with the following Bogoliubov–de Gennes form:

$$H'_{\mathrm{BdG}} = \begin{pmatrix} U + J & 0 \\ 0 & -U + J \end{pmatrix}. \tag{28}$$

Hence the secular determinant of the operator $1 - G(z)H'_{\mathrm{ada}}$, Eq. (25), reduces in the local atomic basis just to a determinant of an ordinary 2×2 matrix. So finally, the in-gap energies $|E| < |\Delta|$ of the perturbed problem satisfy the following (integro-algebraic) secular equation:

$$\mathrm{Re}\{[1 - (U + J)\gamma(E)][1 - (U - J)\gamma(-E)]\} = J\frac{E}{i\sqrt{|\Delta|^2 - E^2}}[\gamma(E) - \gamma(-E)]. \tag{29}$$

Further, using a fact that $\gamma(-E) = \overline{\gamma(E)}$, the left-hand side of the above equation can be expressed as a sum of two terms: $\{1 - (U + J)\,\mathrm{Re}[\gamma(E)]\}\{1 - (U - J)\,\mathrm{Re}[\gamma(E)]\}$ and $(U^2 - J^2)\{\mathrm{Im}[\gamma(E)]\}^2$. We will show in a sequel that at resonances the first of them turns to zero and, correspondingly, the secular equation, Eq. (29), simplifies even more:

$$(U^2 - J^2)\,\mathrm{Im}[\gamma(E)] = 2\frac{EJ}{\sqrt{|\Delta|^2 - E^2}}. \tag{30}$$

Let us recall that the normal-phase *resonant energies* $\mu_\pm$ of the unperturbed host under an action of $H'_{\rm ada}$ are defined [93,95–98] by the following equations:

$$\lim_{\eta\to 0}\int dx\,\frac{(\mu_\pm - x)}{(\mu_\pm - x)^2+\eta^2}\,\varrho_\star(x) = \frac{1}{U\pm J}. \tag{31}$$

In practice, one relaxes infinitesimality of η and uses some fixed value smaller than the corresponding resonance width [96]

$$\Gamma_{c\pm} = \pi\,|U^2 - J^2|\,\varrho_\star(\mu_\pm), \tag{32}$$

which is inversely proportional to the lifetime of the resonance ($\tau_{\rm life} = \hbar/\Gamma_c$). This constraint on the magnitude of η implies that the resonance energies $\mu_\pm$ are given with an uncertainty of $\Gamma_{c\pm}$. Assume we have a superconducting system at the chemical potential μ close to μ_+ or μ_- (within a range of $\Gamma_{c\pm}$) that possesses a superconducting gap Δ, such that $\Gamma_{c\pm} \gtrsim |\Delta| > \sqrt{|\Delta|^2 - E^2}$. Taking the real part of Eq. (27), we can write

$$\mathrm{Re}[\gamma(E)] = \int \frac{dx\,(\mu_\pm - x)\,\varrho_\star(x)}{(\mu_\pm - x)^2 + (|\Delta|^2 - E^2)} \simeq \frac{1}{U\pm J}. \tag{33}$$

This guarantees that the term $\{1-(U+J)\mathrm{Re}[\gamma(E)]\}\{1-(U-J)\mathrm{Re}[\gamma(E)]\} \simeq 0$. Similarly, for the imaginary part of Eq. (27) we get

$$\mathrm{Im}[\gamma(E)] = -\int \frac{dx\,\sqrt{|\Delta|^2 - E^2}\,\varrho_\star(x)}{(\mu_\pm - x)^2 + (|\Delta|^2 - E^2)} \simeq -\pi\varrho_\star(\mu_\pm), \tag{34}$$

where the last equality holds for the unperturbed system with a relatively wide bandwidth and properly varying density of states $\varrho_\star$ on the scale larger than $\Gamma_{c\pm}$. Within these assumptions, the expression for the secular determinant, Eq. (30), finally reads [99]

$$\frac{|E|}{\sqrt{|\Delta|^2 - E^2}} \simeq \frac{\Gamma_{c\pm}}{2|J|} = \frac{1}{2}\frac{\hbar/|J|}{\hbar/\Gamma_{c\pm}} = \frac{1}{2}\frac{\tau_{\rm Larmor}}{\tau_{\rm life}}. \tag{35}$$

The above formula gives the energies of YSR states for a superconducting system whose Fermi level μ is tuned to the vicinity of the normal-phase resonance, i.e., $\mu \simeq \mu_\pm$ within a range of $\Gamma_{c\pm}$. Knowing the resonance width $\Gamma_{c\pm}$ and the strength of magnetic exchange J, or equivalently, the lifetime $\tau_{\rm life}$ of the normal-phase resonance and the Larmor precession time, $\tau_{\rm Larmor} = \hbar/|J|$, due to magnetic exchange J one can easily get the corresponding YSR energies:

$$E_{\rm YSR} = \pm\frac{|\Delta|}{\sqrt{1+4J^2/\Gamma_c^2}} = \pm\frac{|\Delta|}{\sqrt{1+4\tau_{\rm life}^2/\tau_{\rm Larmor}^2}}. \tag{36}$$

Scrutinizing Eqs. (35) and (36) further, we see that whenever the Larmor precession time is substantially smaller than the resonance lifetime the corresponding YSR energies would be very close to the center of the superconducting gap, i.e., $|E| \simeq 0$. Moreover, having two atomic sites—say dimer and nondimer in the case of BLG—out of which the first gives rise to a narrower resonance than the second, then for the same magnetic J the corresponding YSR energies would be deeper inside the gap for the first site than for the second. Our findings are pointing along similar lines as those of the recent study [100] that investigated formation and coupling of the YSR states to a substrate when tuning the Fermi level into the Van Hove singularity.

Based on the above considerations, one can already predict what to expect for the quasiparticles' spin relaxation. Quasiparticles occupy energies above the superconducting gap, while the YSR states carrying magnetic moments are inside the gap. The larger the energy separation is between the two groups, the more "invisible" these states become for each other. Consequently, we expect substantially weakened quasiparticle spin relaxation at chemical potentials that yield YSR states deep inside the superconducting gap. The effect should be more visible when lowering the temperature since there Δ grows with a lowered T according to Eq. (3). Of course, at too low temperatures the spin relaxation quenches naturally because of the absence of free quasiparticle states which rather pair and enter the BCS condensate.

IV. RESULTS

We implemented Hamiltonian $H_{\rm BLG} + H_{\rm ada}$, Eq. (1), for the hydrogen functionalized superconducting BLG in KWANT, and calculated its various transport, relaxation and spectral properties. The very detailed numerical implementation scheme is provided in the Supplemental Material [53] for readers willing to adopt it to other materials or further spintronics applications. We have chosen hydrogen, since it is the most probable and natural atomic contaminant coming from organic solvents used in a sample-fabrication process, and also, because it acts as a resonant magnetic scatterer [57,89]. Of course, methodology as developed can be used for any adatom species that are well described by Hamiltonian $H_{\rm ada}$.

Discussing the results, we start from spectral and spatial properties of YSR states, continue with spin relaxation, and end up with the Andreev spectra and critical currents of the BLG-based Josephson junctions. Moreover, we assume dilute adatom concentrations that do not affect the magnitude of the proximity-induced superconducting gap $|\Delta|$ and do not give it pronounced local spatial variations on the length scale shorter than the coherence length. To make a fully self-consistent approach is beyond the scope of the present paper.

A. Yu-Shiba-Rusinov states

Figure 2(a) compares the YSR spectra for hydrogenated superconducting BLG versus chemical potential computed analytically—solutions of Eq. (25) for the adatom Hamiltonian $H_{\rm ada}$, Eq. (24)—and by direct numerical diagonalization. The obtained spectra by both methods match quantitatively very well for $\Delta_0 = 50$ meV up to a very tiny offset stemming from finite-size effects and fixed convergence tolerance of 10^{-5} in the numerical diagonalization procedure. The main features of the YSR spectra for the gap of 50 meV are clearly visible in Fig. 2(a), and are also reproduced for a smaller gap of 1 meV displayed in Fig. 2(b). The magnetic impurity on the dimer site exhibits two, well-separated, doping regions—around $\mu = -0.1$ eV and $\mu = 0.08$ eV—hosting YSR states with energies deep inside the gap, while the nondimer site supports the low energy YSR states over a much broader doping region. As derived in Sec. III B, deep lying YSR states

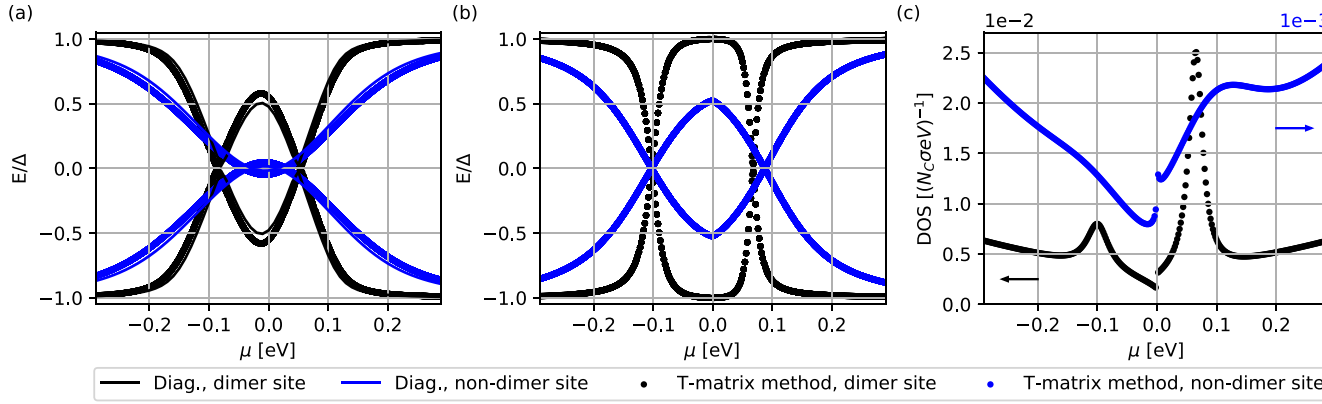

FIG. 2. Spectral comparison—superconducting YSR states and normal-phase resonances in BLG: YSRs' energies in units of Δ vs chemical potential μ for superconducting BLG with the pairing gap $\Delta_0 = 50\,\text{meV}$ (a) and $\Delta_0 = 1\,\text{meV}$ (b) computed analytically (dots) and numerically (lines) for hydrogen magnetic impurity chemisorbed on the dimer (black) and nondimer (blue) site; the results of numerical diagonalization displayed in panel (a) were carried on a rectangular flake with the width $W = 601a$ and length $L = 601a$, and hard-wall boundary conditions. Panel (c) shows perturbed DOS in normal BLG (per carbon atom and spin) vs chemical potential for concentration $\eta_{\text{ada}} = 0.7\,\%$ of dimer (black, units on left axis) and nondimer (blue, units on right axis) magnetic impurities. Positions of the resonance peaks in the normal-phase correspond to the minima of YSR states in panels (a) and (b), in accordance with a prediction in Sec. III B.

should form in resonances, and therefore in Fig. 2(c) we show the analytical DOS for BLG in the normal-phase perturbed by 0.7 % of resonant magnetic impurities—resonance peaks in the DOS match perfectly with "(almost) zero energy" YSR states.

Seeing the YSRs' energies and DOS induced by adatoms at dimer and nondimer sites we can expect certain spectral differences in the corresponding spin relaxations. As mentioned above, the extended quasiparticle states occupy energies over the superconducting gap, while the localized YSR states are inside the gap. The larger is their energy separation, the more "ineffective" is their mutual interaction and hence substantially weakened would be scattering and spin relaxation.

This is quite a general statement irrespective of BLG that is based on the energy overlap argument. However, in the case of BLG what would matter on top of this is the spatial overlap between the localized YSR states and propagating quasiparticle modes within BLG. Figures 3 and 4 show, correspondingly, the sublattice resolved YSR probabilities originating from hydrogen magnetic impurities chemisorbed at dimer and nondimer carbon sites. The plotted eigenstates' probabilities correspond to the YSR spectra in Fig. 2 for the particular chemical potential of $\mu = -0.1\,\text{eV}$ [value at which one of the dimer resonances in the normal system appears; see Fig. 2 (c)]. Inspecting Figs. 3 and 4 we see that for the magnetic impurity chemisorbed on the dimer (nondimer) carbon site in the top layer, the corresponding YSR states dominantly occupy the opposite—nondimer (dimer) top sublattice—of BLG. The spatial profiles of the YSR probability densities with their threefold symmetry matches with the results of the recent study of YSR states in twisted BLG [101].

Moreover, by diagonalizing H_{BdG}, Eq. (14), for μ in $[-\gamma_1, +\gamma_1]$, one sees that the BLG quasiparticle states are built primarily on p_z orbitals belonging to the low-energy $B2$ and $A1$ carbons, i.e., they propagate mainly through the nondimer sublattice of BLG; see Fig. 1. Thus, from a pure geometrical point of view, there is a substantially larger (smaller) spatial overlap between these low-energy BLG states and YSR states originating from the dimer (nondimer) impurities, since the latter spread over the nondimer (dimer) sublattice. Therefore for μ in $[-\gamma_1, +\gamma_1]$, we expect a stronger spin relaxation for magnetic impurities at dimer than nondimer sites.

B. Spin relaxation

In s-wave superconductors, the quasiparticle spin relaxation by nonresonant magnetic impurities follows the conventional Hebel-Slichter picture [39,41,42]. That is, when entering from the normal into the superconducting phase, the spin relaxation rate initially increases due to the superconducting coherence; lowering temperature further it starts to saturate, and by approaching a milli-Kelvin regime the spin relaxation quenches completely due to the lack of quasiparticle excitations.

Figures 5(a) and 5(b) show temperature and doping dependencies of spin relaxation in hydrogenated superconducting BLG with the pairing gap $\Delta_0 = 1\,\text{meV}$. Obviously, we see that the spin relaxation due to resonant magnetic impurities does not follow the Hebel-Slichter picture over the whole ranges of doping. Passing into the superconducting phase the spin relaxation in BLG drops down substantially with lowered T at doping regions around the resonances—particularly, in the dimer case for $\mu \in [-0.2, 0.2]\,\text{eV}$ and in the nondimer one for $\mu \in [-0.4, 0.4]\,\text{eV}$—and enhances at doping levels away from them. The reason for the drop was first elucidated in Ref. [35], and counts the formation of YSR states lying deep inside the superconducting gap. The latter energetically decouple from the quasiparticle ranges, as explained in Sec. III B and documented in Fig. 2. Consequently, the reduced energy overlap between the two groups of states—which gets more pronounced when lowering T and raising $\Delta(T)$ in accordance with Eq. (3)—implies the lowered spin relaxation. In the regions far away from the resonances, the YSR states are close to the gap edges, and the spin relaxation follows the conventional Hebel-Slichter scenario. For the moderate

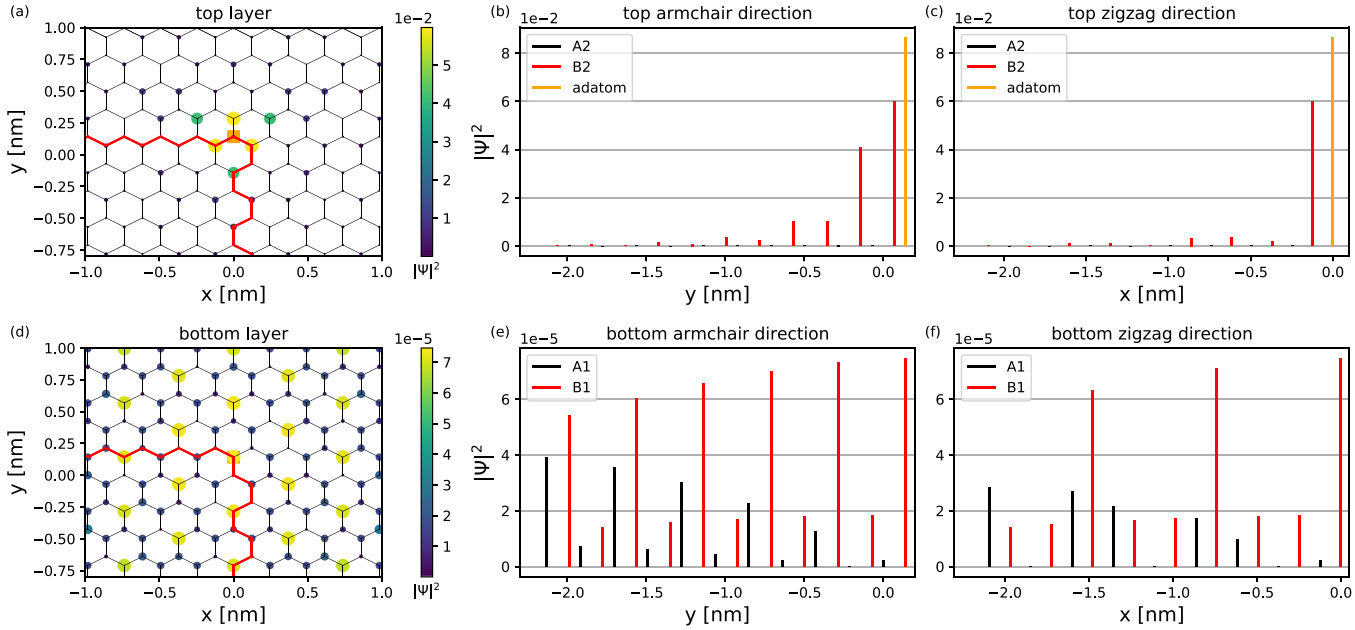

FIG. 3. Sublattice resolved probabilities of YSR states in top (a) and bottom (d) layers originating from a magnetic adatom (hydrogen) chemisorbed at a dimer carbon in the top layer at chemical potential $\mu = -0.1\,\mathrm{eV}$; for the corresponding energy spectrum see Fig. 2. Side panels show sublattice-resolved probabilities in the corresponding layers for two representative directions, armchair [(b), (e)] and zigzag [(c), (f)]. The numerical calculations—exact diagonalization—employed $\Delta_0 = 50\,\mathrm{meV}$, $W = 601a$, and $L = 601a$.

temperatures (above 1 K), the crossover from the resonant to Hebel-Slichter picture in BLG appears around $|\mu| \simeq 0.2\,\mathrm{eV}$ in the dimer case and $|\mu| \simeq 0.4\,\mathrm{eV}$ in the nondimer one.

Impurity spectral features—positions of the resonance peaks and their widths, see Fig. 2(c)—affect doping dependencies of the spin-relaxation rates already in the normal phase [89]. The spin-relaxation rate for the spectrally narrow dimer impurity shows two pronounced shoulders in $1/\tau_s$, see Fig. 5(a), while the spectrally wide nondimer resonance washes out the subpeak structure and producing a single wide hump in Fig. 5(b); of course, this depends on the mutual strengths of the exchange $V_s^{(1)}$ and orbital interaction V_o. For the extended discussion, see Ref. [89]. In reality, the

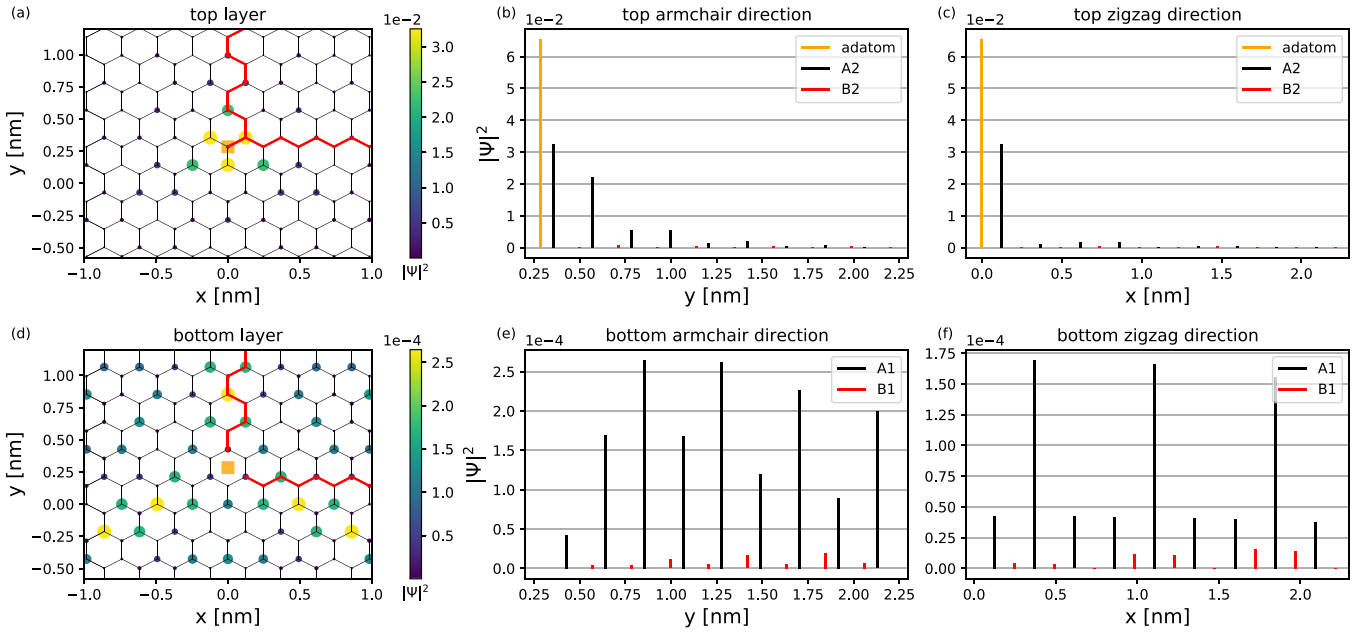

FIG. 4. Sublattice resolved probabilities of YSR states in top (a) and bottom (d) layers originating from a magnetic adatom (hydrogen) chemisorbed at a nondimer carbon in the top layer at chemical potential $\mu = -0.1\,\mathrm{eV}$; for the corresponding energy spectrum, see Fig. 2. Side panels show sublattice-resolved probabilities in the corresponding layers for two representative directions, armchair [(b), (e)] and zigzag [(c), (f)]. The numerical calculations—exact diagonalization—employed $\Delta_0 = 50\,\mathrm{meV}$, $W = 601a$, and $L = 601a$.

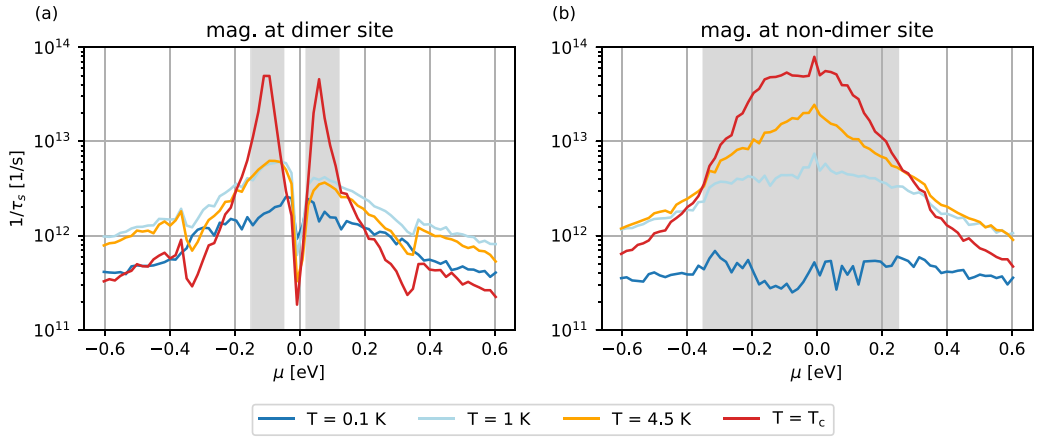

FIG. 5. Quasiparticle spin-relaxation rates in superconducting BLG with $\Delta_0 = 1$ meV for different temperatures T (different colors) as functions of chemical potential μ; the gray shaded backgrounds mark the doping regions at which the system behaves resonantly. Panels (a) and (b) display, correspondingly, spin-relaxation rates for hydrogen magnetic impurity chemisorbed on dimer and nondimer site employing the rate formula given by Eq. (S2). Calculation was performed for BLG Hamiltonian with all γ hoppings involved, the spatial dimensions of the scattering region were fixed to $W = 131\,a$ and $L = 4\,a$, and the phase averaging counted 20 equally spaced values of $k_{\text{trans}}W$ in the interval $[0; 2\pi)$. The impurity concentration for this configuration corresponds to $\eta_{\text{ada}} = 0.0413\,\%$.

spin-relaxation rate would be broadened due to other effects, like electron-hole puddles, variations of orbital parameters with doping and temperature, spatial separation of impurities, etc., so the final rate gets effectively smeared out and its internal shoulder-like structure is not necessarily observed directly [102–105]. In the case of dimer impurity, we see that around $|\mu| \simeq \gamma_1 = 0.3$ eV the spin-relaxation rate slightly jumps up. This is because around this energy the electronic states from high-energy carbons $A2$ and $B1$, see Fig. 1, enter the transport and the number of scattering channels raises. It is worth to compare the magnitudes of spin relaxation rates in Figs. 5(a) and 5(b) for impurities at dimer and nondimer sites when passing from the normal phase at $T_c = 6.953$ K to the superconducting phase at the milli-Kelvin range around $T = 0.1$ K. We see that the dimer impurity relaxes quasiparticles' spins faster than the nondimer one at very low T superconducting phase, but this turns approaching T_c and going into the normal phase. Again, this is the consequence of the wave function overlaps between the extended low-energy quasiparticle BLG modes and the localized YSR states as displayed in Figs. 3 and 4.

In the Appendix, we also show results for the spin-relaxation rates in the case of SOC active hydrogen impurities. As expected, the rates exhibit a strong decrease over the whole doping range when lowering the temperature for both impurity configurations. These findings are consistent with the calculations in single-layer graphene [35].

C. Critical current of the BLG-based Josephson junction

Figure 6 illustrates the critical currents of the BLG-based Josephson junctions as functions of chemical potential for different lengths and different hydrogen positions. We study junctions functionalized with the dimer and nondimer resonant magnetic impurities (data displayed by black or blue), as well as a junction without them (data in gray); for a junction schematic, see the inset in Fig. 6. In the latter benchmark case, we just plot the critical current for $L = 20a$, as the length dependence is not affecting the magnitude of I_c too strongly. Comparing the scaling of the critical current I_c with the chemical potential μ for the dimer and nondimer impurity cases, we see that I_c drops its value at those doping levels where the BLG system in the normal phase hits its resonances; for comparison see DOS in Fig. 2(c). The effect is more pronounced for the narrow resonance in the dimer case, but also the nondimer impurity displays a wide plateau in I_c that is spreading over its resonance width.

We see that I_c for the nondimer case is lower than I_c for the dimer one, implying the system is more perturbed by the res-

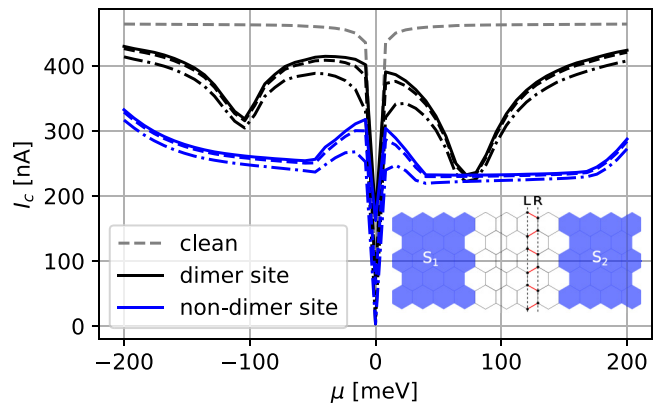

FIG. 6. Critical currents of the BLG-based Josephson junctions (see inset for schematics) with and without resonant magnetic impurities calculated by Eq. (S4). Data for different lengths are displayed by different styles—the full lines corresponds to length $L = 10a$, the dashed lines to $L = 20a$ and the dashed-dotted lines to $L = 60a$. Different colors code different impurity contents—the clean junction result is displayed by gray, and data for a junction with a single hydrogen in its center at dimer (nondimer) site by black (blue). The width of the junctions is fixed to $W = 40a$, and the pairing gap Δ_0 in the BLG-based superconducting leads equals 1 meV.

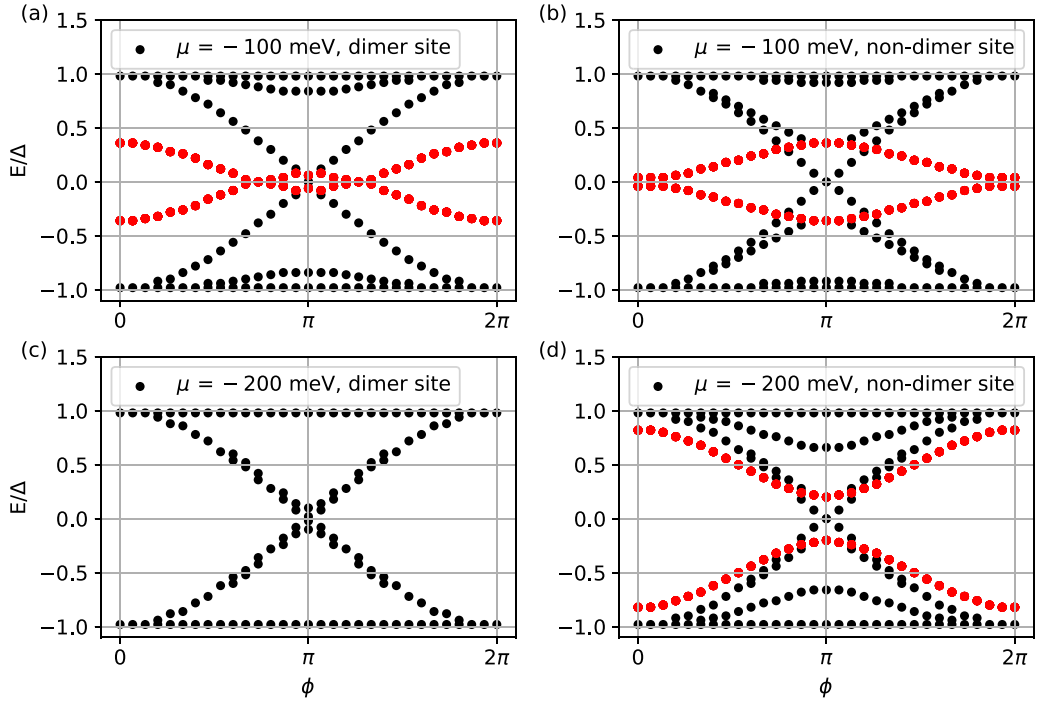

FIG. 7. ABS spectra of BLG-based Josephson junction functionalized by resonant magnetic impurities. Panels (a) and (b) show correspondingly the ABS spectra for a hydrogen impurity at dimer and nondimer site at chemical potential $\mu = -100\,\text{meV}$ (resonance), while panels (c) and (d) correspond to the same configuration at doping level $\mu = -200\,\text{meV}$ (off-resonance for the dimer impurity). Bound state energies are obtained by sampling maximas of $d(E)$, Eq. (S3), for energies E inside the superconducting gap. The size of the normal spacer has width $W = 40a$ and length $L = 10a$ and contains a single impurity positioned in the center. Bands shown in red correspond to ABS that result from the interplay of the magnetic exchange and the superconducting pairing and share certain spectral similarities with the YSR states.

onant scattering off magnetic impurities chemisorbed on the nondimer sites. For the same reason, the spin relaxation rate $1/\tau_s$ for the nondimer position in the normal phase ($T = T_c$) is larger than the corresponding quantity for the dimer one; see Figs. 5. The explanation of why this happens was given in Ref. [89]: An impurity chemisorbed at the nondimer (dimer) site gives rise to a resonant impurity state in the normal phase that is located on the dimer (nondimer) sublattice—similarly as for the YSR states; see Figs. 3 and 4. However, there is one substantial difference compared with the localized YSR states. The resonant levels are virtually bound, meaning their spatial probability falls off with a distance polynomially [106,107]. Since the top dimer sublattice of BLG couples via γ_1 hopping with the bottom layer, the effect of resonant state living on the dimer top sublattice would be felt also on the bottom layer. While the both layers are affected by the resonance, the scattering is more damaging—this is the reason for the larger $1/\tau_s$ and smaller I_c in the normal phase for the impurity located on the nondimer site. In contrast, the resonant state due to the dimer impurity, which is located on the nondimer top sublattice of BLG, would only weakly protrude into the bottom layer—nondimer carbons do not hybridize via γ_1—and hence an electron propagating in BLG is effectively less scattered off the dimer impurities since the bottom layer gives it a green light to move freely.

So we believe that the Josephson current spectroscopy can serve as another sensible probe for discriminating between different resonant impurities reflecting their spectral and resonant features.

D. Andreev bound state spectrum of BLG-based Josephson junction

Figure 7 shows the Andreev in-gap spectra for the BLG-based Josephson junction functionalized by dimer-nondimer hydrogen impurities as functions of the phase difference ϕ. We consider the same geometry and system sizes (width $W = 40a$ and length $L = 10a$) as were used for the calculation of the critical currents in Fig. 6. Moreover, we calculate the ABS spectra for the two representative chemical potentials, $\mu = -100\,\text{meV}$ and $\mu = -200\,\text{meV}$, that set different resonant regimes.

Figures 7(a) and 7(b) display the corresponding ABS energies for $\mu = -100\,\text{meV}$ at which both chemisorption positions host resonances in the normal phase. The first remarkable feature in the spectra for both impurity positions is the presence of the ABS bands (shown in red) that are detached from the continuum spectrum and spread around the center of the gap. This is very similar to the YSR spectra shown in Fig. 2, where at the same doping level μ develops the YSR bound states whose energies are located close to the center of the gap. Because of this spectral similarity, one can consider the red ABS as Josephson-junction descendants of the corresponding YSR states, despite, strictly speaking, the YSR states being defined for impurities embedded directly inside a superconductor and not inside the normal spacer of the Josephson junction. Comparing closely the dimer [Fig. 7(a)] and nondimer [Fig. 7(b)] parts, we see also the black dotted ABS with the typical Andreev ϕ dispersions determined mainly by the junction length L and the S/N-interface

TABLE I. Hamiltonian parameters.

Hydrogen	Dimer [eV]	Nondimer [eV]
ϵ	0.25	0.35
ω	6.5	5.5
J	-0.4	-0.4
λ_I^A	-0.21×10^{-3}	-0.21×10^{-3}
λ_I^B	0	0
λ_R	0.33×10^{-3}	0.33×10^{-3}
λ_{PIA}^A	0	0
λ_{PIA}^B	0.77×10^{-3}	0.77×10^{-3}

transparency [108,109]. We assume a transparent junction realized, for example, on a flake of BLG that is proximitized by two superconductors with different phases which are separated by a nonproximitized normal region. Contrasting the slopes of red and black ABS branches for both chemisorption positions, we see that in the nondimer case the slopes of the red and black bands are mostly opposite, implying a suppression of the critical current since $I(\phi) \propto \sum_{\mathrm{ABS}} \partial E^{\mathrm{ABS}}(\phi)/\partial\phi$.

Next, let us change the chemical potential to the lower value of $\mu = -200\,\mathrm{meV}$, such that the dimer site is already out of the resonance, while the nondimer one is still "in a mild shadow" of it; see the DOS features in Fig. 2(c). The corresponding ABS spectra are displayed in Figs. 7(c) and 7(d). In contrast to the previous cases, the ABS "resembling" the YSR states are absent (more precisely overlying with other branches) for the dimer case, but are still optically visible for the nondimer one—again displayed in red, although now spreading energetically more away the center of the gap. The remaining bound state energies—displayed by black—resemble the standard ABS dispersions. So off resonances the magnetic impurities in the normal spacer act on the formation of the ABS as nonmagnetic scatterers. In the Supplemental Material [53], we also provide a comparison to a different calculation approach with switched off magnetic moments in order to cross-check the employed numerics.

V. CONCLUSIONS

In summary, we have shown that the superconducting BLG in the presence of resonant magnetic impurities experiences interesting spin phenomena that are manifested in (1) an unusual doping and temperature dependency of spin-relaxation rates, (2) subgap spectra hosting deep-lying YSR states, (3) magnitudes of critical currents, and (4) Andreev bound states in the BLG-based Josephson junctions. BLG has two nonequivalent sublattices; hence, the same magnetic adatom hybridizing with BLG can show differing superconducting behavior. Our secondary aim was to trace these features in detail and understand their origins from the point of view of resonant scattering in the normal BLG phase.

Coming to the spin relaxation, we have convincingly demonstrated by implementing an S-matrix approach that it can depart from the conventional Hebel-Slichter scenario when taking into account the multiple scattering processes. Meaning, the quasiparticle spin-relaxation rates can substantially decrease once the system is turned into the superconducting phase. Furthermore, the detailed numerical implementation scheme we have developed using the existing KWANT functionalities—see the Supplemental Material [53]—represents *per se* an important message. It allows us to simulate spin relaxation, as well as other spectral characteristics including the YSR and Andreev bound states.

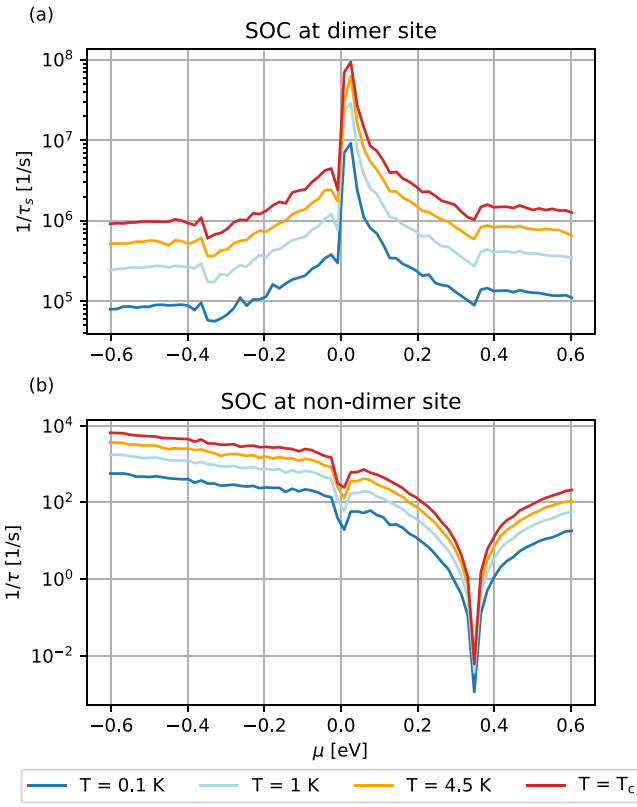

FIG. 8. Temperature dependence of the quasiparticle spin-relaxation rates vs doping for superconducting BLG in the presence of a spin-orbit active hydrogen impurity at dimer and nondimer sites. Results are obtained from KWANT simulations with the help of Eq. (S2). The system size was fixed to W $= 131a$ and L $= 4$a, giving $\eta_{ada} = 0.0413\,\%$. The phase averaging was performed for 20 equally spaced values of k_{trans} in the interval $[0; 2\pi]$.

Beyond the BLG, we have demonstrated under general conditions that at doping levels that are tuned to the normal-state resonances, the corresponding YSR states separate from the quasiparticle coherence peaks and immerse deep in the center of the gap, or even cross there. Such zero-energy YSR states have a profound impact on the topological nature of the underlying superconducting ground state with practical applications for the YSR [49,110–112] and Josephson spectroscopy [113], as well on the Shiba-band engineering, particularly in connection with topological quantum-phase transitions and parity changing of the condensate wave function [109,114–116]. We derived a formula, Eq. (36), for the YSR energies assuming the system is doped in resonance. Knowing the resonant width of the modified DOS and the strength of the exchange coupling, one can predict with the help of Eq. (36) the YSR energies, or vice versa, knowing the width from normal-phase transport measurements and the YSR energies from the STM one can estimate a magnitude of

the exchange strength between itinerant electrons and localized magnetic moments.

We are not aware of any experiments probing spin relaxation in superconducting graphene or BLG, but we believe that our results can trigger some, or can shed some light on the similar superspintronics phenomena explored in other low-dimensional superconductors.

ACKNOWLEDGMENTS

This work was supported by Deutsche Forschungsgemeinschaft (DFG, German Research Foundation) within Project ID No. 314695032-SFB 1277 (Project A07) and the Elitenetzwerk Bayern Doktorandenkolleg "Topological Insulators". D.K. acknowledges partial support from the project SUPERSPIN funded by Slovak Academy of Sciences via the initiative IMPULZ 2021. We thank Marco Aprili, Andreas Costa, Ferdinand Evers, Jaroslav Fabian, Richard Hlubina, Tomáš Novotný, and Klaus Richter for useful discussions.

APPENDIX: MODEL PARAMETERS, LOCAL SOC HAMILTONIAN, AND THE CORRESPONDING SPIN RELAXATION

An external impurity hybridizing with BLG modifies a part of the orbital degrees of freedom, Hamiltonian V_o, and the local SOC environment. To investigate the impact of the local SOC on the quasiparticle spin relaxation, we use the following tight-binding Hamiltonian:

$$
\begin{aligned}
V_s^{(2)} = {} & \frac{i\lambda_I^A}{3\sqrt{3}} \sum_{m\in \mathrm{C_{nnn}}} \sum_{\sigma} c_{0\sigma}^{\dagger} (\hat{s}_z)_{\sigma\sigma} c_{m\sigma} + \mathrm{H.c.} + \frac{i\lambda_I^B}{3\sqrt{3}} \sum_{\substack{m,n\in \mathrm{C_{nn}} \\ m\neq n}} \sum_{\sigma} c_{m\sigma}^{\dagger}\, \nu_{mn} (\hat{s}_z)_{\sigma\sigma} c_{n\sigma} \\
& + \frac{2i\lambda_R}{3} \sum_{m\in \mathrm{C_{nn}}} \sum_{\sigma\neq\sigma'} c_{0\sigma}^{\dagger} (\hat{\boldsymbol{s}} \times \boldsymbol{d}_{0m})_{z,\sigma\sigma'} c_{m\sigma'} + \mathrm{H.c.} + \frac{2i\lambda_{\mathrm{PIA}}^A}{3} \sum_{m\in \mathrm{C_{nnn}}} \sum_{\sigma\neq\sigma'} c_{0\sigma}^{\dagger} (\boldsymbol{d}_{0m} \times \hat{\boldsymbol{s}})_{z,\sigma\sigma'} c_{m\sigma'} + \mathrm{H.c.} \\
& + \frac{2i\lambda_{\mathrm{PIA}}^B}{3} \sum_{\substack{m,n\in \mathrm{C_{nn}} \\ m\neq n}} \sum_{\sigma\neq\sigma'} c_{m\sigma}^{\dagger} (\boldsymbol{d}_{mn} \times \hat{\boldsymbol{s}})_{z,\sigma\sigma'} c_{n\sigma'};
\end{aligned}
$$

for details see Ref. [88].

The parameters entering Hamiltonians V_o, $V_s^{(1)}$, and $V_s^{(2)}$ that are used in this study correspond to hydrogen impurity; the values are obtained from fitting DFT calculations [84,89] and are summarized in Table I. Figure 8 shows quasiparticle spin-relaxation rates versus doping for a spin-orbit active hydrogen impurity, again for several representative temperatures going from the critical T_c down to zero. The relaxation rate shows clear differences for the dimer, Fig. 8(a), and the nondimer, Fig. 8(b) positions. While the dimer case displays a strong enhancement of the rate around $\mu = 0$, the rate is heavily suppressed in the nondimer case for $\mu = 0.34\,\mathrm{eV}$. These features remain insensitive to the variation of temperature and transcend also into the superconducting-phase. Passing from the normal to superconducting regime, we observe a global reduction of the spin-relaxation rate by an order of magnitude. This observations match with the results obtained for superconducting single layer graphene [35].

[1] I. Žutić, J. Fabian, and S. Das Sarma, Spintronics: Fundamentals and applications, Rev. Mod. Phys. **76**, 323 (2004).
[2] W. Han, R. K. Kawakami, M. Gmitra, and J. Fabian, Graphene spintronics, Nat. Nanotechnol. **9**, 794 (2014).
[3] S. Roche, J. Åkerman, B. Beschoten, J.-C. Charlier, M. Chshiev, S. Prasad Dash, B. Dlubak, J. Fabian, A. Fert, M. Guimarães, F. Guinea, I. Grigorieva, C. Schönenberger, P. Seneor, C. Stampfer, S. O. Valenzuela, X. Waintal, and B. van Wees, Graphene spintronics: The European Flagship perspective, 2D Mater. **2**, 030202 (2015).
[4] A. Avsar, H. Ochoa, F. Guinea, B. Özyilmaz, B. J. van Wees, and I. J. Vera-Marun, Colloquium: Spintronics in graphene and other two-dimensional materials, Rev. Mod. Phys. **92**, 021003 (2020).
[5] I. Žutić, A. Matos-Abiague, B. Scharf, H. Dery, and K. Belashchenko, Proximitized materials, Mater. Today **22**, 85 (2019).
[6] V. Podzorov, M. E. Gershenson, C. Kloc, R. Zeis, and E. Bucher, High-mobility field-effect transistors based on transition metal dichalcogenides, Appl. Phys. Lett. **84**, 3301 (2004).
[7] W. Shi, J. Ye, Y. Zhang, R. Suzuki, M. Yoshida, J. Miyazaki, N. Inoue, Y. Saito, and Y. Iwasa, Superconductivity series in transition metal dichalcogenides by ionic gating, Sci. Rep. **5**, 12534 (2015).
[8] S. Jo, D. Costanzo, H. Berger, and A. F. Morpurgo, Electrostatically induced superconductivity at the surface of WS 2, Nano Lett. **15**, 1197 (2015).
[9] E. Navarro-Moratalla, J. O. Island, S. Mañas-Valero, E. Pinilla-Cienfuegos, A. Castellanos-Gomez, J. Quereda, G. Rubio-Bollinger, L. Chirolli, J. A. Silva-Guillén, N. Agraït, G. A. Steele, F. Guinea, H. S. J. van der Zant, and E. Coronado, Enhanced superconductivity in atomically thin TaS_2, Nat. Commun. **7**, 11043 (2016).
[10] D. Costanzo, S. Jo, H. Berger, and A. F. Morpurgo, Gate-induced superconductivity in atomically thin MoS_2 crystals, Nat. Nanotechnol. **11**, 339 (2016).
[11] A. G. Swartz, P. M. Odenthal, Y. Hao, R. S. Ruoff, and R. K. Kawakami, Integration of the ferromagnetic insulator EuO onto graphene, ACS Nano **6**, 10063 (2012).
[12] H. X. Yang, A. Hallal, D. Terrade, X. Waintal, S. Roche, and M. Chshiev, Proximity Effects Induced in Graphene by

Magnetic Insulators: First-Principles Calculations on Spin Filtering and Exchange-Splitting Gaps, Phys. Rev. Lett. **110**, 046603 (2013).

[13] J. B. S. Mendes, O. Alves Santos, L. M. Meireles, R. G. Lacerda, L. H. Vilela-Leão, F. L. A. Machado, R. L. Rodríguez-Suárez, A. Azevedo, and S. M. Rezende, Spin-Current to Charge-Current Conversion and Magnetoresistance in a Hybrid Structure of Graphene and Yttrium Iron Garnet, Phys. Rev. Lett. **115**, 226601 (2015).

[14] P. Wei, S. Lee, F. Lemaitre, L. Pinel, D. Cutaia, W. Cha, F. Katmis, Y. Zhu, D. Heiman, J. Hone, J. S. Moodera, and C.-T. Chen, Strong interfacial exchange field in the graphene/EuS heterostructure, Nat. Mater. **15**, 711 (2016).

[15] A Dyrdał and J. Barnaś, Anomalous, spin, and valley Hall effects in graphene deposited on ferromagnetic substrates, 2D Mater. **4**, 034003 (2017).

[16] A. Hallal, F. Ibrahim, H. Yang, S. Roche, and M. Chshiev, Tailoring magnetic insulator proximity effects in graphene: First-principles calculations, 2D Mater. **4**, 025074 (2017).

[17] J. F. Sierra, J. Fabian, R. K. Kawakami, S. Roche, and S. O. Valenzuela, Van der Waals heterostructures for spintronics and opto-spintronics, Nat. Nanotechnol. **16**, 856 (2021).

[18] Y. Cao, V. Fatemi, S. Fang, K. Watanabe, T. Taniguchi, E. Kaxiras, and P. Jarillo-Herrero, Unconventional superconductivity in magic-angle graphene superlattices, Nature (London) **556**, 43 (2018).

[19] M. Yankowitz, S. Chen, H. Polshyn, Y. Zhang, K. Watanabe, T. Taniguchi, D. Graf, A. F. Young, and C. R. Dean, Tuning superconductivity in twisted bilayer graphene, Science **363**, 1059 (2019).

[20] M. Eschrig, Spin-polarized supercurrents for spintronics, Phys. Today **64**, 43 (2011).

[21] M. Eschrig, Spin-polarized supercurrents for spintronics: A review of current progress, Rep. Prog. Phys. **78**, 104501 (2015).

[22] J. Linder and J. W. A. Robinson, Superconducting spintronics, Nat. Phys. **11**, 307 (2015).

[23] G. Yang, C. Ciccarelli, and J. W. A. Robinson, Boosting spintronics with superconductivity, APL Mater. **9**, 050703 (2021).

[24] H. B. Heersche, P. Jarillo-Herrero, J. B. Oostinga, L. M. K. Vandersypen, and A. F. Morpurgo, Bipolar supercurrent in graphene, Nature (London) **446**, 56 (2007).

[25] K. Komatsu, C. Li, S. Autier-Laurent, H. Bouchiat, and S. Guéron, Superconducting proximity effect in long superconductor/graphene/superconductor junctions: From specular Andreev reflection at zero field to the quantum Hall regime, Phys. Rev. B **86**, 115412 (2012).

[26] V. E. Calado, S. Goswami, G. Nanda, M. Diez, A. R. Akhmerov, K. Watanabe, T. Taniguchi, T. M. Klapwijk, and L. M. K. Vandersypen, Ballistic Josephson junctions in edge-contacted graphene, Nat. Nanotechnol. **10**, 761 (2015).

[27] D. I. Indolese, R. Delagrange, P. Makk, J. R. Wallbank, K. Wanatabe, T. Taniguchi, and C. Schönenberger, Signatures of Van Hove Singularities Probed by the Supercurrent in a Graphene-hBN Superlattice, Phys. Rev. Lett. **121**, 137701 (2018).

[28] K. Li, X. Feng, W. Zhang, Y. Ou, L. Chen, K. He, L.-L. Wang, L. Guo, G. Liu, Q.-K. Xue, and X. Ma, Superconductivity in Ca-intercalated epitaxial graphene on silicon carbide, Appl. Phys. Lett. **103**, 062601 (2013).

[29] B. M. Ludbrook, G. Levy, P. Nigge, M. Zonno, M. Schneider, D. J. Dvorak, C. N. Veenstra, S. Zhdanovich, D. Wong, P. Dosanjh, C. Straßer, A. Stöhr, S. Forti, C. R. Ast, U. Starke, and A. Damascelli, Evidence for superconductivity in Li-decorated monolayer graphene, Proc. Natl. Acad. Sci. USA **112**, 11795 (2015).

[30] J. Chapman, Y. Su, C. A. Howard, D. Kundys, A. N. Grigorenko, F. Guinea, A. K. Geim, I. V. Grigorieva, and R. R. Nair, Superconductivity in Ca-doped graphene laminates, Sci. Rep. **6**, 23254 (2016).

[31] C. Tonnoir, A. Kimouche, J. Coraux, L. Magaud, B. Delsol, B. Gilles, and C. Chapelier, Induced Superconductivity in Graphene Grown on Rhenium, Phys. Rev. Lett. **111**, 246805 (2013).

[32] A. Di Bernardo, O. Millo, M. Barbone, H. Alpern, Y. Kalcheim, U. Sassi, A. K. Ott, D. De Fazio, D. Yoon, M. Amado, A. C. Ferrari, J. Linder, and J. W. A. Robinson, *p*-wave triggered superconductivity in single-layer graphene on an electron-doped oxide superconductor, Nat. Commun. **8**, 14024 (2017).

[33] J. R. Schrieffer, *Theory of Superconductivity* (Benjamin, New York, 1964)

[34] Y. Yafet, Conduction electron spin relaxation in the superconducting state, Phys. Lett. A **98**, 287 (1983).

[35] D. Kochan, M. Barth, A. Costa, K. Richter, and J. Fabian, Spin Relaxation in *s*-wave Superconductors in the Presence of Resonant Spin-Flip Scatterers, Phys. Rev. Lett. **125**, 087001 (2020).

[36] H. Yang, S.-H. Yang, S. Takahashi, S. Maekawa, and S. S. P. Parkin, Extremely long quasiparticle spin lifetimes in superconducting aluminium using MgO tunnel spin injectors, Nat. Mater. **9**, 586 (2010).

[37] F. Hübler, M. J. Wolf, D. Beckmann, and H. V. Löhneysen, Long-Range Spin-Polarized Quasiparticle Transport in Mesoscopic Al Superconductors with a Zeeman Splitting, Phys. Rev. Lett. **109**, 207001 (2012).

[38] C. H. L. Quay, M. Weideneder, Y. Chiffaudel, C. Strunk, and M. Aprili, Quasiparticle spin resonance and coherence in superconducting aluminium, Nat. Commun. **6**, 8660 (2015).

[39] L. C. Hebel and C. P. Slichter, Nuclear relaxation in superconducting aluminum, Phys. Rev. **107**, 901 (1957).

[40] N. Poli, J. P. Morten, M. Urech, A. Brataas, D. B. Haviland, and V. Korenivski, Spin Injection and Relaxation in a Mesoscopic Superconductor, Phys. Rev. Lett. **100**, 136601 (2008).

[41] L. C. Hebel and C. P. Slichter, Nuclear spin relaxation in normal and superconducting aluminum, Phys. Rev. **113**, 1504 (1959).

[42] L. C. Hebel, Theory of nuclear spin relaxation in superconductors, Phys. Rev. **116**, 79 (1959).

[43] D. C. Cavanagh and B. J. Powell, Fate of the Hebel-Slichter peak in superconductors with strong antiferromagnetic fluctuations, Phys. Rev. Research **3**, 013241 (2021).

[44] L. Yu, Bound state in superconductors with paramagnetic impurities, Acta Phys. Sin. **21**, 75 (1965).

[45] H. Shiba, Classical spins in superconductors, Prog. Theor. Phys. **40**, 435 (1968).

[46] A. I. Rusinov, Superconductivity near a paramagnetic impurity, Zh. Eksp. Teor. Fiz. **9**, 146 (1968) [JETP Lett. **9**, 85 (1969)].

[47] T. O. Wehling, H. P. Dahal, A. I. Lichtenstein, and A. V. Balatsky, Local impurity effects in superconducting graphene, Phys. Rev. B **78**, 035414 (2008).

[48] J. L. Lado and J. Fernández-Rossier, Unconventional Yu-Shiba-Rusinov states in hydrogenated graphene, 2D Mater. **3**, 025001 (2016).

[49] E. Cortés-del Río, J. L. Lado, V. Cherkez, P. Mallet, J.-Y. Veuillen, J. C. Cuevas, J. M. Gómez-Rodríguez, J. Fernández-Rossier, and I. Brihuega, Observation of Yu–Shiba–Rusinov states in superconducting graphene, Adv. Mater. **33**, 2008113 (2021).

[50] T. O. Wehling, S. Yuan, A. I. Lichtenstein, A. K. Geim, and M. I. Katsnelson, Resonant Scattering by Realistic Impurities in Graphene, Phys. Rev. Lett. **105**, 056802 (2010).

[51] S. Irmer, D. Kochan, J. Lee, and J. Fabian, Resonant scattering due to adatoms in graphene: Top, bridge, and hollow positions, Phys. Rev. B **97**, 075417 (2018).

[52] Y. G. Pogorelov, V. M. Loktev, and D. Kochan, Impurity resonance effects in graphene versus impurity location, concentration, and sublattice occupation, Phys. Rev. B **102**, 155414 (2020).

[53] See Supplemental Material at http://link.aps.org/supplemental/10.1103/PhysRevB.105.205409 including Refs. [35,54–78], for detailed explanations of the numerical calculations and additional information regarding the employed model.

[54] C. W. Groth, M. Wimmer, A. R. Akhmerov, and X. Waintal, KWANT: A software package for quantum transport, New J. Phys. **16**, 063065 (2014).

[55] J. Bundesmann, D. Kochan, F. Tkatschenko, J. Fabian, and K. Richter, Theory of spin-orbit-induced spin relaxation in functionalized graphene, Phys. Rev. B **92**, 081403(R) (2015).

[56] J. Katoch, T. Zhu, D. Kochan, S. Singh, J. Fabian, and R. K. R. Kawakami, Transport Spectroscopy of Sublattice-Resolved Resonant Scattering in Hydrogen-Doped Bilayer Graphene, Phys. Rev. Lett. **121**, 136801 (2018).

[57] D. Kochan, S. Irmer, M. Gmitra, and J. Fabian, Resonant Scattering by Magnetic Impurities as a Model for Spin Relaxation in Bilayer Graphene, Phys. Rev. Lett. **115**, 196601 (2015).

[58] M. Mashkoori, K. Björnson, and A. Black-Schaffer, Impurity bound states in fully gapped d-wave superconductors with subdominant order parameters, Sci. Rep. **7**, 44107 (2017).

[59] J. W. Eaton, D. Bateman, S. Hauberg, and R. Wehbring, *GNU Octave Version 6.1.0 Manual: A High-Level Interactive Language for Numerical Computations* (2020).

[60] A. F. Andreev, Electron spectrum of the intermediate state of superconductors, Soviet Phys. JETP **22**, 455 (1966).

[61] I. O. Kulik and A. N. Omel'yanchuk, Properties of superconducting microbridges in the pure limit, Sov. J. Low Temp. Phys. (Engl. Transl.); (United States) **3**, 459 (1977).

[62] J. A. Sauls, Andreev bound states and their signatures, Philos. Trans. R. Soc. A **376**, 20180140 (2018).

[63] B. Josephson, Possible new effects in superconductive tunnelling, Phys. Lett. **1**, 251 (1962).

[64] B. D. Josephson, The discovery of tunnelling supercurrents, Rev. Mod. Phys. **46**, 251 (1974).

[65] M. Titov and C. W. J. Beenakker, Josephson effect in ballistic graphene, Phys. Rev. B **74**, 041401(R) (2006).

[66] W. A. Muñoz, L. Covaci, and F. M. Peeters, Tight-binding study of bilayer graphene Josephson junctions, Phys. Rev. B **86**, 184505 (2012).

[67] M. Alidoust, M. Willatzen, and A.-P. Jauho, Symmetry of superconducting correlations in displaced bilayers of graphene, Phys. Rev. B **99**, 155413 (2019).

[68] M. Alidoust, A.-P. Jauho, and J. Akola, Josephson effect in graphene bilayers with adjustable relative displacement, Phys. Rev. Research **2**, 032074(R) (2020).

[69] P. Sriram, S. S. Kalantre, K. Gharavi, J. Baugh, and B. Muralidharan, Supercurrent interference in semiconductor nanowire Josephson junctions, Phys. Rev. B **100**, 155431 (2019).

[70] A. Furusaki, DC Josephson effect in dirty SNS junctions: Numerical study, Phys. B: Condens. Matter **203**, 214 (1994).

[71] V. P. Ostroukh, B. Baxevanis, A. R. Akhmerov, and C. W. J. Beenakker, Two-dimensional Josephson vortex lattice and anomalously slow decay of the Fraunhofer oscillations in a ballistic SNS junction with a warped Fermi surface, Phys. Rev. B **94**, 094514 (2016).

[72] K. Zuo, V. Mourik, D. B. Szombati, B. Nijholt, D. J. van Woerkom, A. Geresdi, J. Chen, V. P. Ostroukh, A. R. Akhmerov, S. R. Plissard, D. Car, E. P. A. M. Bakkers, D. I. Pikulin, L. P. Kouwenhoven, and S. M. Frolov, Supercurrent Interference in Few-Mode Nanowire Josephson Junctions, Phys. Rev. Lett. **119**, 187704 (2017).

[73] J. W. McClure, Band structure of graphite and de Haas–van Alphen effect, Phys. Rev. **108**, 612 (1957).

[74] J. C. Slonczewski and P. R. Weiss, Band structure of graphite, Phys. Rev. **109**, 272 (1958).

[75] S. Konschuh, M. Gmitra, D. Kochan, and J. Fabian, Theory of spin-orbit coupling in bilayer graphene, Phys. Rev. B **85**, 115423 (2012).

[76] E. McCann and M. Koshino, The electronic properties of bilayer graphene, Rep. Prog. Phys. **76**, 056503 (2013).

[77] C. W. J. Beenakker, Universal Limit of Critical-Current Fluctuations in Mesoscopic Josephson Junctions, Phys. Rev. Lett. **67**, 3836 (1991).

[78] B. van Heck, S. Mi, and A. R. Akhmerov, Single fermion manipulation via superconducting phase differences in multiterminal Josephson junctions, Phys. Rev. B **90**, 155450 (2014).

[79] M. Tinkham, *Introduction to Superconductivity*, 2nd ed., Dover Books on Physics (Dover, New York, 2004).

[80] J. I.-J. Wang, L. Bretheau, D. Rodan-Legrain, R. Pisoni, K. Watanabe, T. Taniguchi, and P. Jarillo-Herrero, Tunneling spectroscopy of graphene nanodevices coupled to large-gap superconductors, Phys. Rev. B **98**, 121411(R) (2018).

[81] J. Li, H.-B. Leng, H. Fu, K. Watanabe, T. Taniguchi, X. Liu, C.-X. Liu, and J. Zhu, Superconducting proximity effect in a transparent van der Waals superconductor-metal junction, Phys. Rev. B **101**, 195405 (2020).

[82] G.-H. Lee and H.-J. Lee, Proximity coupling in superconductor-graphene heterostructures, Rep. Prog. Phys. **81**, 056502 (2018).

[83] However, in special cases that involved numerical diagonalization, we use even larger $\Delta_0 = 50\,\mathrm{meV}$ just to reach convergence and cross-check analytical results.

[84] M. Gmitra, D. Kochan, and J. Fabian, Spin-Orbit Coupling in Hydrogenated Graphene, Phys. Rev. Lett. **110**, 246602 (2013).

[85] S. Irmer, T. Frank, S. Putz, M. Gmitra, D. Kochan, and J. Fabian, Spin-orbit coupling in fluorinated graphene, Phys. Rev. B **91**, 115141 (2015).

[86] K. Zollner, T. Frank, S. Irmer, M. Gmitra, D. Kochan, and J. Fabian, Spin-orbit coupling in methyl functionalized graphene, Phys. Rev. B **93**, 045423 (2016).

[87] T. Frank, S. Irmer, M. Gmitra, D. Kochan, and J. Fabian, Copper adatoms on graphene: Theory of orbital and spin-orbital effects, Phys. Rev. B **95**, 035402 (2017).

[88] D. Kochan, S. Irmer, and J. Fabian, Model spin-orbit coupling Hamiltonians for graphene systems, Phys. Rev. B **95**, 165415 (2017).

[89] D. Kochan, M. Gmitra, and J. Fabian, Spin Relaxation Mechanism in Graphene: Resonant Scattering by Magnetic Impurities, Phys. Rev. Lett. **112**, 116602 (2014).

[90] A. C. Hewson, *The Kondo Problem to Heavy Fermions*, Cambridge Studies in Magnetism (Cambridge University Press, Cambridge, UK, 1993).

[91] D. Kochan, M. Gmitra, and J. Fabian, Resonant scattering off magnetic impurities in graphene: Mechanism for ultrafast spin relaxation, in *Symmetry, Spin Dynamics, and the Properties of Nanostructures: Lecture Notes of the 11th International School on Theoretical Physics, Rzeszów, Poland, 1–6 September 2014*, edited by J. Barnaś, V. Dugaev, and A. Wal (World Scientific Publishing, Singapore, 2014), pp. 136–162.

[92] A. V. Balatsky, I. Vekhter, and J.-X. Zhu, Impurity-induced states in conventional and unconventional superconductors, Rev. Mod. Phys. **78**, 373 (2006).

[93] I. M. Lifshitz, S. A. Gredescul, and L. A. Pastur, *Introduction to the Theory of Disordered Systems* (Wiley-VCH, Berlin, 1988).

[94] As a comment, while in this toy model we assume no macroscopic spin polarization and no spin-orbit interaction in the unperturbed system, we employ the reduced Nambu formalism. However, one should keep in mind that for any solution with an energy E the full Nambu-space approach will give as a solution also the energy $-E$.

[95] M. Lifšic, Some problems of the dynamic theory of non-ideal crystal lattices, Nuovo Cimento **3**, 716 (1956).

[96] P. W. Anderson, Localized magnetic states in metals, Phys. Rev. **124**, 41 (1961).

[97] I. M. Lifshitz, The energy spectrum of disordered systems, Adv. Phys. **13**, 483 (1964).

[98] R. J. Elliott, J. A. Krumhansl, and P. L. Leath, The theory and properties of randomly disordered crystals and related physical systems, Rev. Mod. Phys. **46**, 465 (1974).

[99] A very similar formula (unpublished) was obtained using a different perspective; T. Novotný (private communication).

[100] M. Uldemolins, A. Mesaros, and P. Simon, Effect of Van Hove singularities on Shiba states in two-dimensional s-wave superconductors, Phys. Rev. B **103**, 214514 (2021).

[101] A. Lopez-Bezanilla and J. L. Lado, Defect-induced magnetism and Yu-Shiba-Rusinov states in twisted bilayer graphene, Phys. Rev. Materials **3**, 084003 (2019).

[102] W. Han and R. K. Kawakami, Spin Relaxation in Single-Layer and Bilayer Graphene, Phys. Rev. Lett. **107**, 047207 (2011).

[103] T.-Y. Yang, J. Balakrishnan, F. Volmer, A. Avsar, M. Jaiswal, J. Samm, S. R. Ali, A. Pachoud, M. Zeng, M. Popinciuc, G. Güntherodt, B. Beschoten, and B. Özyilmaz, Observation of Long Spin-Relaxation Times in Bilayer Graphene at Room Temperature, Phys. Rev. Lett. **107**, 047206 (2011).

[104] J. Ingla-Aynés, M. H. D. Guimarães, R. J. Meijerink, P. J. Zomer, and B. J. van Wees, 24-μm spin relaxation length in boron nitride encapsulated bilayer graphene, Phys. Rev. B **92**, 201410(R) (2015).

[105] A. Avsar, I. J. Vera-Marun, J. Y. Tan, G. K. W. Koon, K. Watanabe, T. Taniguchi, S. Adam, and B. Özyilmaz, Electronic spin transport in dual-gated bilayer graphene, NPG Asia Mater. **8**, e274 (2016).

[106] V. M. Pereira, F. Guinea, J. M. B. Lopes dos Santos, N. M. R. Peres, and A. H. Castro Neto, Disorder Induced Localized States in Graphene, Phys. Rev. Lett. **96**, 036801 (2006).

[107] E. V. Castro, M. P. López-Sancho, and M. A. H. Vozmediano, New Type of Vacancy-Induced Localized States in Multilayer Graphene, Phys. Rev. Lett. **104**, 036802 (2010).

[108] I. O. Kulik, Macroscopic quantization and the proximity effect in S-N-S junctions, Zh. Eksp. Teor. Fiz **57**, 1745 (1970) [Sov. Phys. JETP **30**, 944 (1970)].

[109] A. Costa, J. Fabian, and D. Kochan, Connection between zero-energy Yu-Shiba-Rusinov states and 0-π transitions in magnetic Josephson junctions, Phys. Rev. B **98**, 134511 (2018).

[110] G. C. Ménard, S. Guissart, C. Brun, S. Pons, V. S. Stolyarov, F. Debontridder, M. V. Leclerc, E. Janod, L. Cario, D. Roditchev, P. Simon, and T. Cren, Coherent long-range magnetic bound states in a superconductor, Nat. Phys. **11**, 1013 (2015).

[111] B. W. Heinrich, J. I. Pascual, and K. J. Franke, Single magnetic adsorbates on s-wave superconductors, Prog. Surf. Sci. **93**, 1 (2018).

[112] D. Wang, J. Wiebe, R. Zhong, G. Gu, and R. Wiesendanger, Spin-Polarized Yu-Shiba-Rusinov States in an Iron-Based Superconductor, Phys. Rev. Lett. **126**, 076802 (2021).

[113] F. Küster, A. M. Montero, F. S. M. Guimarães, S. Brinker, S. Lounis, S. S. P. Parkin, and P. Sessi, Correlating Josephson supercurrents and Shiba states in quantum spins unconventionally coupled to superconductors, Nat. Commun. **12**, 1108 (2021).

[114] A. Sakurai, Comments on superconductors with magnetic impurities, Prog. Theor. Phys. **44**, 1472 (1970).

[115] J. D. Sau and E. Demler, Bound states at impurities as a probe of topological superconductivity in nanowires, Phys. Rev. B **88**, 205402 (2013).

[116] F. Pientka, Y. Peng, L. Glazman, and F. von Oppen, Topological superconducting phase and Majorana bound states in Shiba chains, Phys. Scr. **T164**, 014008 (2015).